Salt Flows in the Central Red Sea

Peter Feldens and Neil C. Mitchell

Abstract

The central Red Sea is a nascent oceanic basin. Miocene evaporites, kilometers in thickness, were deposited during its continental rifting phase and early seafloor spreading. With further seafloor spreading, increasing dissolution due to increasing hydrothermal circulation as well as normal fault movements removed lateral constraint of the evaporites at the walls of the axial rift valley. Because halite is a ductile material that forms a large part of the evaporite sequence, the evaporites started to move downslope, passively carrying their hemipelagic sediment cover. Today, flowlike features comprising Miocene evaporites are situated on the top of younger magnetic seafloor spreading anomalies. Six salt flows, most showing rounded fronts in plan view, with heights of several hundred meters and widths between 3 and 10 km, are identified by high-resolution bathymetry and DSDP core material around Thetis Deep and Atlantis II Deep, and between Atlantis II Deep and Port Sudan Deep. The relief of the underlying volcanic basement likely controls the positions of individual salt flow lobes. On the flow surfaces, along-slope and downslope ridge and trough morphologies parallel to the local seafloor gradient have developed, presumably due to extension of the hemiplegic sediment cover or strike-slip movement within the evaporites. A few places of irregular seafloor topography are observed close to the flow fronts, interpreted to be the result of dissolution of Miocene evaporites, which contributes to the formation of brines in several of the deeps. Based on the vertical relief of the flow lobes, deformation is taking place in the upper part of the evaporite sequence. Considering a salt flow at Atlantis II Deep in more detail, strain rates due to dislocation creep and pressure solution creep were estimated to be 10^{-14} 1/s and 10^{-10} 1/s, respectively, using given assumptions of grain size and deforming layer thickness. The latter strain rate, comparable to strain rates observed for onshore salt flows in Iran, results in flow speeds of several mm/year for the offshore salt flows in certain locations. Thus, salt flow movements can potentially keep up with Arabia–Nubia tectonic half-spreading rates reported for large parts of the Red Sea.

Introduction

Halite is a ductile material that already deforms under low differential stresses. In response to gravitational stresses, it can form allochthonous salt sheets (Hudec and Jackson 2007). (We use the term "salt" here in the loose sense commonly used in petroleum geology, to signify originally evaporitic sequences whose rheology is strongly dependent on their halite components.) Recent as well as past allochthonous salt sheets from the onshore and offshore environment are known from more than 35 basins worldwide (Hudec and Jackson 2006), including in Iran, Tunisia,

P. Feldens (✉)
Institute of Geosciences, Kiel University, Otto-Hahn Platz 1, 24118 Kiel, Germany
e-mail: pfeldens@geophysik.uni-kiel.de

N.C. Mitchell
School of Earth, Atmospheric and Environmental Sciences, University of Manchester, Williamson Building, Oxford Road, Manchester M13 9PL, UK

Algeria, Germany, Morocco, Canada, South America, Khazakstan, Ukraine, Yemen, Australia, and the Gulf of Mexico (Mohr et al. 2007). For the most part, the sources of allochthonous salt sheets are salt diapirs extruding toward the surface (Hudec and Jackson 2007). Allochthonous salt sheets may be found beneath the surface, either completely or partly buried by clastic sediments, or have spread directly at the surface without a cover of siliciclastic sediments (Hudec and Jackson 2006; Talbot and Pohjola 2009). The latter is the case in Iran, where the best preserved onshore extrusive salt sheets, originally called "salt glaciers" (Lees 1927) are located. However, to avoid redundancy (Talbot and Pohjola 2009), we use the term salt flow (Mitchell et al. 2010). The viscous fluidlike behavior of the Iranian salt flows is dominated by the weak rheology of their halite component (comparable to the behavior of ice glaciers) (Talbot and Pohjola 2009) and results in flow speeds of cm/year to dm/day during surges (Jackson and Talbot 1986).

However, not all salt flows are related to extruding diapirs. Instead, salt flows may develop where evaporites have lost their lateral constraint, observed for evaporites deposited in basins during the continental rifting phase predating the onset of seafloor spreading, for example in the early Atlantic Ocean (Pautot et al. 1966). These evaporites, now situated off the coasts of Africa and South America (Talbot 1993), form important barriers for migrating hydrocarbons. Thus, the early behavior of these evaporites may be of economical interest but is poorly known, as the salt has since been covered by thick siliciclastic sequences, lowering the resolution of acoustic imaging techniques. Further, the salt has been subsequently remobilized and deformed.

The Red Sea serves as an analog of the situation of the early Atlantic Ocean: Here, evaporites were deposited during the Miocene in a continental rift valley (Stoffers and Kühn 1974; Girdler and Whitmarsh 1974). With the onset of seafloor spreading, evaporites overlying the spreading center were dissolved due to hydrothermal circulation, volcanism, and direct contact with seawater during the continuing spreading. In combination with normal fault movements, the evaporites adjacent to the spreading center lost their lateral constraint, and moved downslope due to differential stress exerted by their own weight and the weight of the sedimentary roof. The existence of mobile salt flows situated along the Red Sea spreading axis was already suggested several decades ago (Girdler and Whitmarsh 1974). This suggestion was based on Miocene evaporites that were encountered overlying younger oceanic crust which was identified by its magnetic properties. Corresponding morphologic evidence for salt flows was recently described (Mitchell et al. 2010) at the walls of Thetis Deep. Thus, the Red Sea offers the opportunity to study recent submarine salt flows close to the seafloor surface, especially in the walls of the deeps along the central Red Sea.

High-resolution bathymetric data along the central Red Sea trough became recently available (Schmidt et al. 2011; Ligi et al. 2012). This chapter will explore the available bathymetric data along the Central Red Sea spreading center (Fig. 1) and highlight the typical morphology associated with salt flows in the Red Sea. Further, some basic constraints on flow speed and speculations on deformation mechanisms acting within the salt are developed.

Regional Setting

The Red Sea is currently transitioning from continental to oceanic rifting. Continental rifting is still observed in its northern part, while recently formed oceanic seafloor is observed in the south and within several deeps along the central Red Sea, presumably developed since the Pliocene (Coleman 1993). Detailed information on the opening of the Red Sea and its current structure is given in the articles by Bosworth (this volume), Ligi et al. (this volume), and Ehrhardt (this volume) and by Coleman (1993). In the central Red Sea, evaporites were deposited prior to seafloor spreading, during the Miocene, in the continental rifting phase (Girdler and Whitmarsh 1974). Several seawater incursions left sequences of clay and carbonate deposits. Subsequent evaporation produced evaporites that mainly comprise halite and anhydrite (Stoffers and Kühn 1974; Coleman 1993). Throughout the sequence, interbedded volcanic material exists (Stoffers and Kühn 1974). Evaporite deposition ended approximately with the onset of seafloor spreading. The upper surface of the evaporites is recognized basinwide as a distinct reflector in reflection seismic data ("S-Layer"; Coleman 1993). The thickness of the evaporites reaches 3–4 km in places (Mitchell et al. 1992; Coleman 1993). Based on seismic refraction experiments, the thickness of the evaporites adjacent to the axial trough at the latitude of the Thetis deeps still exceeds 1 km (Tramontini and Davies 1969; Mitchell et al. 2010; Mitchell, this volume), but the nature of the crust beneath those near-trough evaporites is still under discussion. The evaporites are covered by few hundred meters of hemipelagic sediment (Ross and Schlee 1973).

Salt Flows Along the Red Sea Spreading Axis

Observations

Within Thetis Deep (Fig. 2), located at 22°30′ N 37°46′ E, Mitchell et al. (2010) described several key features of submarine salt flow morphology. Generally, the center of Thetis Deep shows a rough morphology including several cone-shaped and ridgelike volcanic structures. In contrast, the walls of the Thetis Deep have a less rugose appearance.

Fig. 1 Overview of high-resolution bathymetric data available in the central Red Sea between Port Sudan Deep, Atlantis II Deep, and Thetis Deep, overlying low-resolution bathymetry. The simplified stratigraphy of the Deep Sea Drilling (DSDP) Sites 225 and 227, including the upper part of the evaporite sequence, is displayed
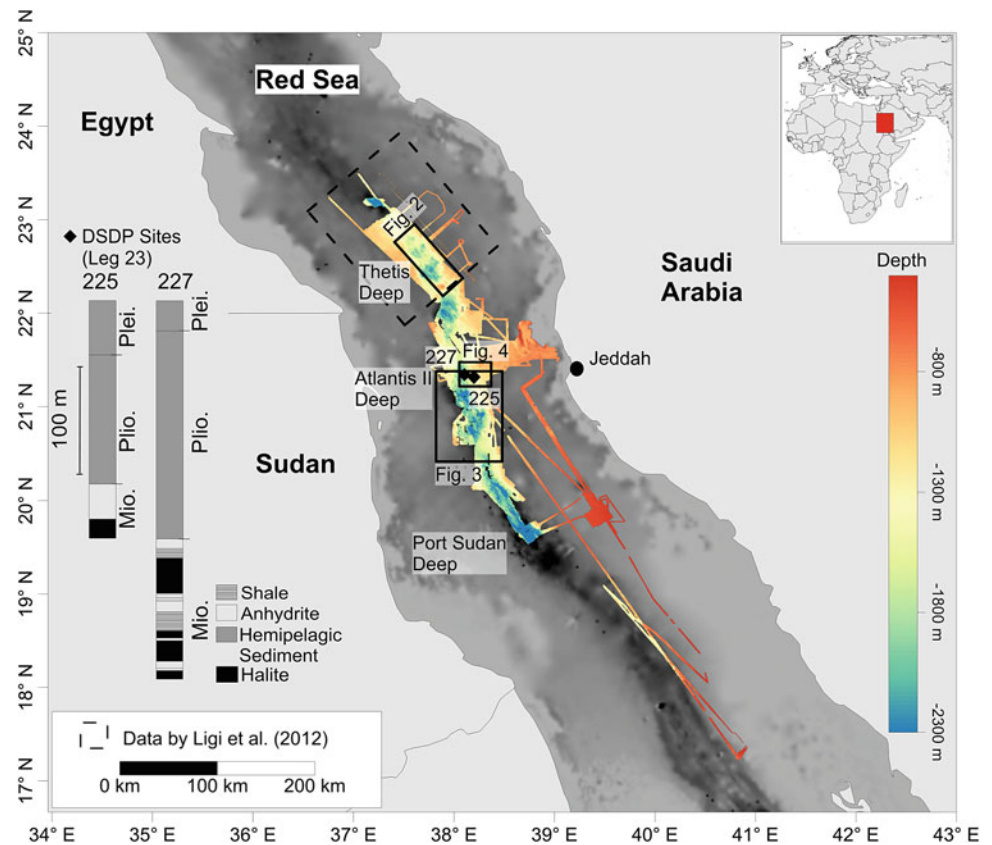
Here, three rounded flow fronts ("A," "B," and "C" in Fig. 2) are recognized. Features B and C protrude from the eastern wall into Thetis Deep, while feature A is located at the northeast boundary to the northern intertrough zone. At features B and C, separate flow lobes can be observed. The widths of the fronts are approximately 3 km at A and 10 km at B and C. Relief heights of the flow front are on the order of 200–500 m. The flow lobes exhibit several steps corresponding to the steps in the adjacent volcanic basement (Fig. 2). Downslope ridges and troughs exist with wavelengths of approximately 1 km and are oriented parallel to the direction of maximum seafloor gradient (Fig. 2). Partly curved fabrics are observed (Fig. 2). Along slope, the ridges and troughs have wavelengths of approximately 200–500 m and heights of less than 20 m (Fig. 2). Along- and downslope ridges are partly superimposed. Mitchell et al. (2010) observed an area of increased seafloor roughness within an embayment of one of the flow lobes.

Morphology similar to the salt flows in Thetis Deep exists further south along the Red Sea spreading axis. An example is displayed in Fig. 3 for the area between 21.3° N and 20.5° N, showing the axial trough and its eastern wall. The central axial trough is characterized by rough seafloor, exhibiting a multitude of cone-shaped volcanic structures and faults that are mainly oriented SE–NW. Compared to most of the central trough, the sedimentary seafloor surface at its eastern

side appears smooth. Three features with rounded fronts (white "D," "E," and "F" in Fig. 3) are recognized. Due to incomplete bathymetric data, their upslope extents (outside the central axial trough) are not known. The widths of the fronts, parallel to the axial trough, are approximately 15 km for feature D, 9 km for feature E, and 5 km for feature F. In the south, volcanic structures occur on the along-slope sides of flowlike features D and E and rise to elevations above the flows (for example, where profiles B–B′ and C–C′ cross). Downslope ridge and trough morphology, with amplitudes in the range of 10–30 m and wavelengths of 400–500 m are notably observed in the narrow section of feature D, which lies between two volcanic features (see profile D–D′). To the south of feature D, the amplitude increases to a maximum of 100 m. Near the rounded front, surface lineaments appear to rotate toward the northwest. Although difficult to determine due to the rough topography, the elevation of the distal part of feature D against the surrounding volcanic basement is approximately 500 m at its southern end and 600 m at its northern end (profile A–A′). A prominent cone-shaped volcano, rising approximately 600 m, is situated between flowlike features D and E (where profiles C–C′ and B–B′ cross). Notably, several curved ridges, convex toward the east, with heights of approximately 15 m, are observed directly toward the east of the volcano (best observed south of "E" in Fig. 3). Feature E itself exhibits a stepwise
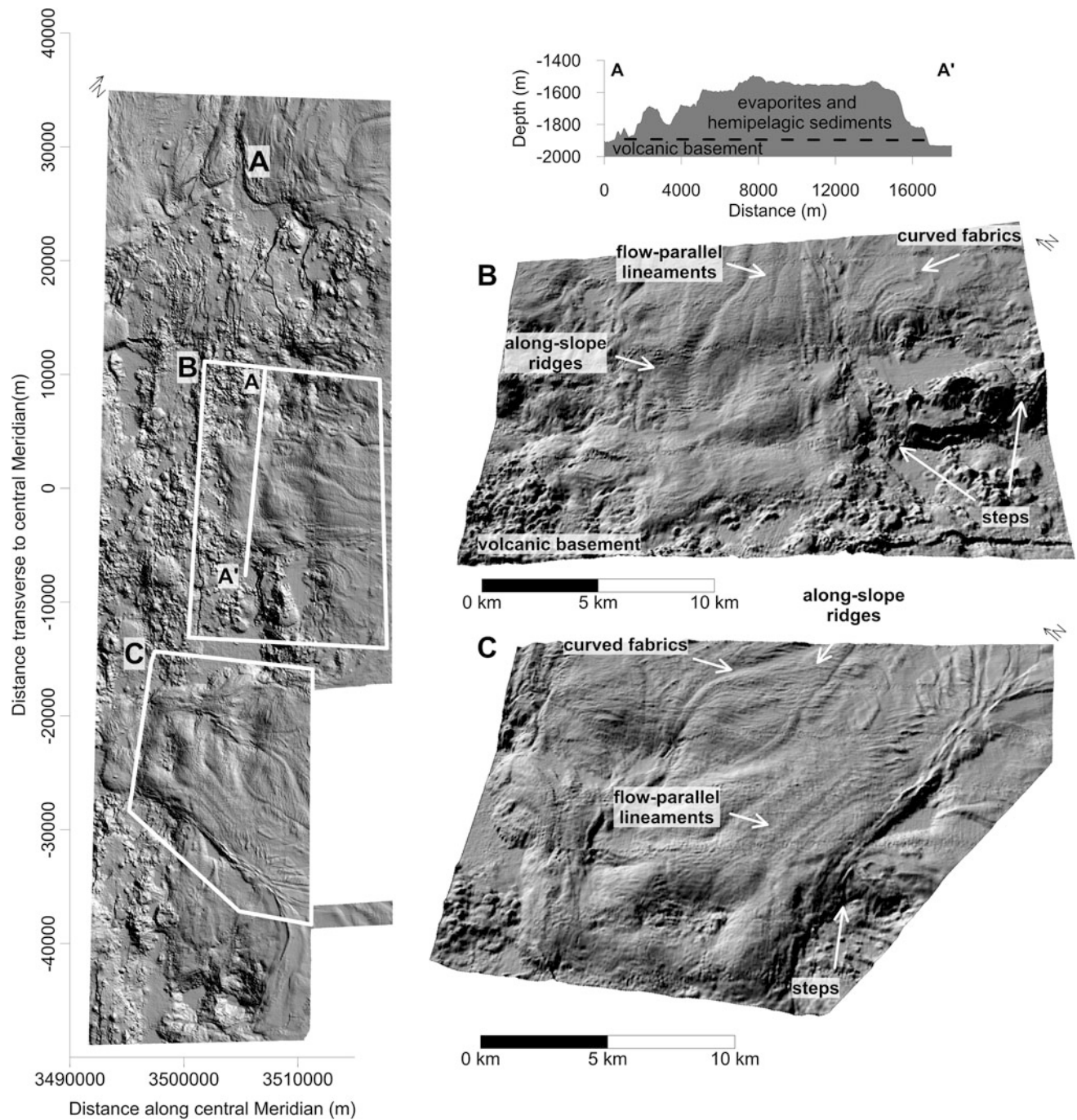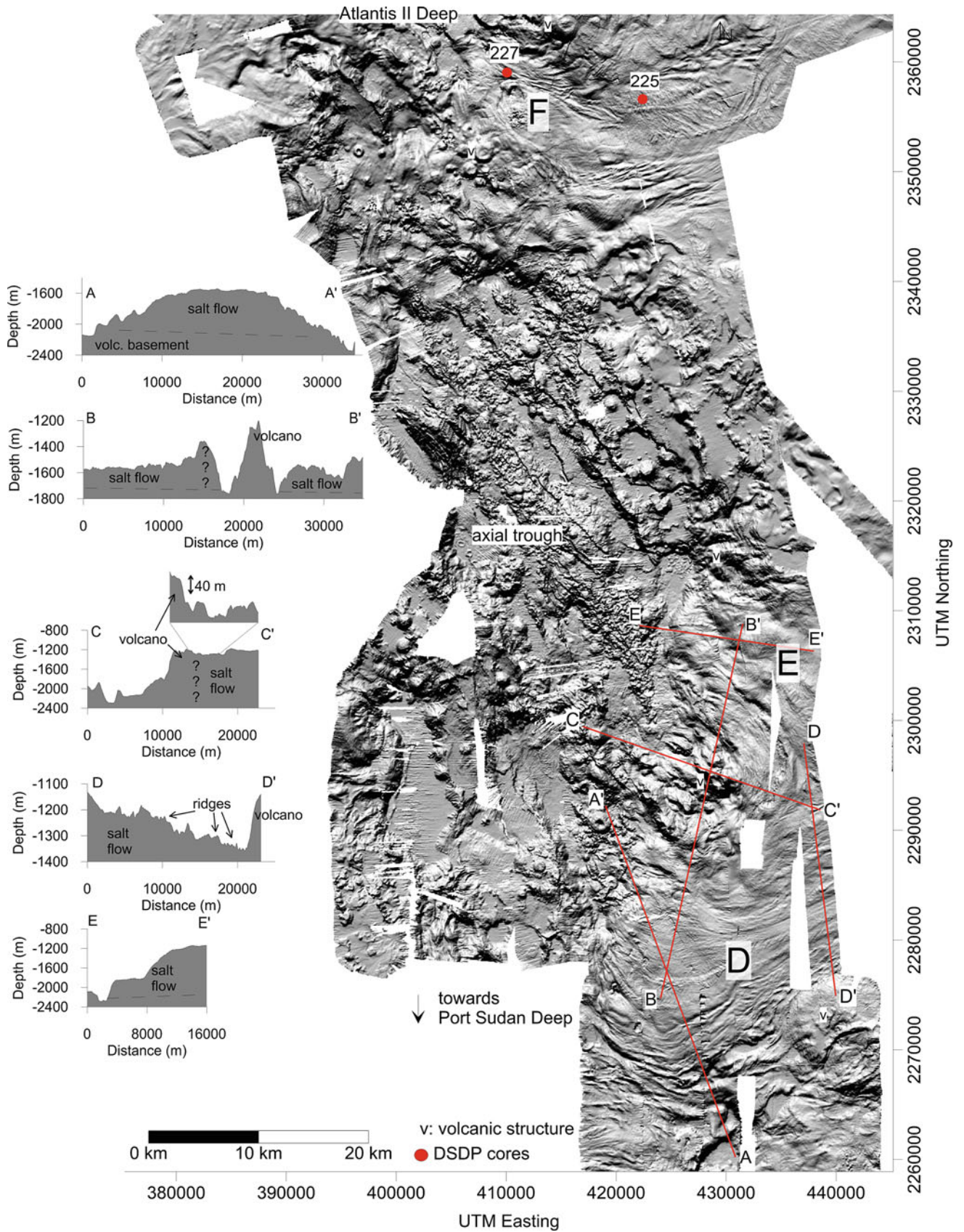
Fig. 2 Shaded relief image of multibeam data in the Thetis Deep (multibeam data of Ligi et al. 2012). Image resolution is 25 m, *vertical exaggeration* of the insets *B,* and *C* is 2:1. Illumination is from 216°/86°. Projected in oblique Mercator projection with the *central line* defined by the coordinates 38.33° N/23.14° E and 37.06° N/22.05° E. Three flowlike features *A, B,* and *C* are identified. Refer to text for further discussion of morphological features

morphology; the contact with the volcanic basement is situated at approximately 2,250 m, the first step rises to 1,800 m, and the second rises to a depth of 1,200 m (profile E–E′, Fig. 3).

Feature F is situated directly at the southeastern wall of the famous Atlantis II Deep (Fig. 3, detailed view in Fig. 4),

located approximately 125 km south of the Thetis Deep. A major difference between Thetis Deep and Atlantis II Deep is the existence of highly saline brine within the latter (Schmidt et al., this volume). The formation of the brine is connected to local hydrothermal circulation cells that cause a partial dissolution of Miocene evaporites (Anschutz and Blanc 1995).

Fig. 3 Shaded relief image of multibeam data south of Atlantis II Deep. Three flowlike features *D*, *E,* and *F* are recognized

Fig. 4 *Top* Three-dimensional image of the southeastern wall of Atlantis II Deep. Vertical exaggeration is 6:1. Magnetic data display anomalies beneath the evaporites recovered from DSDP Site 227. The magnetic data and associated databases are available from the National Geophysical Data Center, National Oceanic and Atmospheric Administration, US Department of Commerce, http://www.ngdc.noaa.gov/. *Bottom* Shaded relief image of the proximal part of the salt flow. Close to the brine filling Atlantis II Deep, irregular morphology is observed. The depth of the brine level is taken from Hartmann et al. (1998). Illumination is from 346°/39°. The vertical exaggeration is 2:1
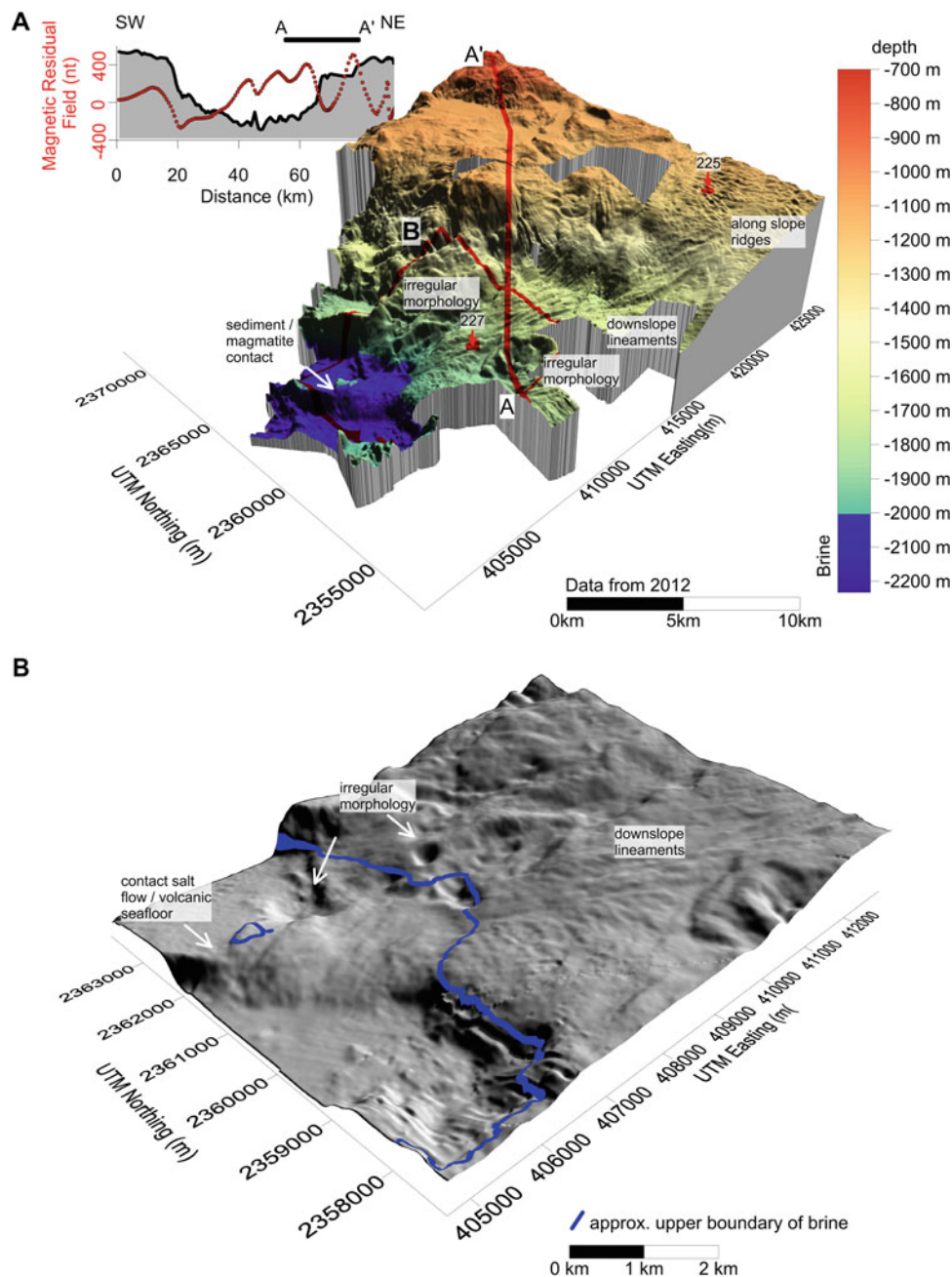
Atlantis II Deep is characterized by a set of NW–SE-directed faults, and cone-shaped volcanic features are frequently observed (Figs. 3 and 4). Arguably, the rounded outline of feature F is more diffuse and difficult to recognize than features D and E. Again, the distal part of feature F, situated between two areas of elevated volcanic basement, exhibits distinct downslope ridge and trough morphology with wavelengths of 200–400 m and elevations of 20 m at maximum. The ridge and trough morphology fades out at the contact to the volcanic basement (Fig. 3). With a depth of approximately 2008 m below sea level (Hartmann et al. 1998; Schmidt et al., this volume), the brine–seawater interface is located slightly above the sediment/volcanic seafloor contact (Fig. 4). At approximately the same depth, irregular seafloor topography (Fig. 4) is observed. Along-slope ridges and troughs are observed at the more proximal part of feature F (at DSDP Site 225 in Figs. 3 and 4). Along-slope and downslope ridges appear partly superimposed. For the most part, along-slope ridges have heights between 10 and 20 m, with wavelengths of approximately 300–500 m. Steps in the volcanic basement morphology continue beneath feature F (to the east of "F" in Fig. 3).

During the DSDP program in the early 1970s (DSDP Leg 23), several sites were drilled (Figs. 1 and 3) at the location

of feature F. The recovered cores show that the top of the Miocene evaporite sequence lies at a depth below seafloor of approximately 150–200 m beneath a cover of partially deformed hemipelagic sediments. Magnetic data (Fig. 3, Izzeldin 1987) indicate that magnetic anomalies are present beneath the area covered by evaporites today (Fig. 4).

Identification of Evaporite Flows

The interpretation of the lobate-shaped sedimentary features at the walls of Thetis Deep as salt flows by Mitchell et al. (2010) was based on the combined analysis of seismic and bathymetric data. Headwalls, which are generally indicative of abrupt slope failures (e.g., Völker et al. 2011; Krastel et al. 2012), are absent in the walls of the Red Sea deeps. A volcanic origin of the flowlike features is rejected based on observed folded layering in seismic data. Additionally, the relief of the flowlike features A to C is larger than the hemipelagic sediment thickness, indicating that evaporites are part of the observed flow lobes. Thus, features A to C are interpreted as being caused by moving evaporites, passively carrying the hemipelagic sediments above them. The hypothesis may be made that the features D, E, and F are related to salt movement as well. By themselves, the morphological similarity to the salt flows observed at Thetis Deep might be only a coincidence, but at Atlantis II Deep, the DSDP cores clearly demonstrate an evaporite origin. The occurrence of only minor deformation of hemipelagic sediment samples with DSDP cores 225 and 227 (Girdler and Whitmarsh 1974) and the absence of headwalls show that no large-scale slope failures exist at the site of feature F. While older low-amplitude magnetic anomalies in the northern Red Sea may relate to mafic intrusions (Cochran 1983), the magnetic anomalies in the Atlantis II Deep were previously interpreted to result from seafloor spreading. At 21° and 22° N, magnetic anomalies include at least anomalies 2A and 2, respectively (Izzeldin 1987; Chu and Gordon 1998), corresponding to the Pliocene/Pleistocene epoch (Mankinen and Dalrymple 1979). The magnetic anomalies are situated beneath the evaporites sampled at the base of DSDP Sites 225 and 227 that are of Miocene age (Stoffers and Kühn 1974; see also Fig. 4). Therefore, it appears reasonable that evaporite flowage occurs at Atlantis II Deep, and generally these flows exhibit a characteristic morphology, including rounded fronts, downslope and along-slope ridge and trough features, escarpments in the volcanic basement that continue beneath the salt flows, as well as irregular topography that resembles dissolution structures. Unfortunately, no geophysical data are available over features D and E (Fig. 3), but the structures are also interpreted as salt flows based on their morphological similarities to the Thetis Deep salt flows.

Morphology Related to Salt Flows

The morphology of the hemipelagic cover on top of the moving evaporites includes downslope ridges and troughs, along-slope ridges, areas of rough topography, as well as steplike morphology at the flow fronts.

Downslope ridge and trough morphologies ("flowstripes") are observed in many regimes of fast ice flow worldwide (Campbell et al. 2008), but the physical explanation for their origin is unclear (Gudmundsson et al. 1998; Glasser and Gudmundsson 2012). Within ice glaciers, such flowstripes form as a response to either subglacial morphology within fast-flowing glaciers, shear margins—for example due to converging ice flows—or to lateral compression due to narrowing cross sections (Bindschadler 1998; Glasser and Gudmundsson 2012). No converging salt flows are observed based on the available bathymetric data. The transfer of subglacial undulations through ice glaciers involves fast glacier flow and basal slippage (Glasser and Gudmundsson 2012), while in salt flows frictional boundaries dominate (Talbot and Pohjola 2009). Furthermore, flowstripes transferring from subglacial basins commonly have wavelengths of at least the glacier's thickness. For the downslope ridges at feature F, this is not the case. However, both lateral compression and increasing flow velocity downflow cause longitudinal extension (Glasser and Gudmundsson 2012). Such behavior may be observed at sites D and F. At D, the flow narrows between rising volcanic basement; at F, the number of downslope ridges increases directly beneath a step of the flow surface. The downslope ridges may also be related to strike-slip movements in the evaporite caused by the rough topography expected at the base of the flows, similar to nunataks observed in glaciology. At least some of the lineaments may be explained by strike-slip movements, as strike-slip-like features have been observed in seismic data of the Thetis Deep and separate flow lobes are observed at the flow fronts at B and C (Mitchell et al. 2010, see also Fig. 2).

In this regard, the partly observed along-slope ridges approximately parallel to the central trough may be created due to extension of the hemipelagic cover, for example, related to changing morphology of the subflow basement. Similar features were observed during submarine spreading following landslides (Micaleff et al. 2007), where sediment extends due to underlying, deforming material, and an along-slope ridge and trough morphology is created where shear stresses exceed the strength of strata, which then separate into individual blocks. However, such morphology is not always observed in the vicinity of steps in the flow surface. A reason may be that extension is not always accommodated by formation of individual blocks, but by thinning of the hemipelagic cover (Mitchell et al. 2010).

While the origin of the downslope and along-slope ridges observed on the proposed salt flows cannot be definitely resolved, their striking morphological similarity, where present, with features observed on ice glaciers or related to submarine mass movement indicates that sediment flow actually takes place in the vicinity of the Red Sea central trough. Hence, these observations reinforce the interpretation of features D and E as salt flows. The salt flow at D and E seems to be steered by the local volcanic basement. For example, the prominent volcano at the cross section of C–C′ and B–B′ (Fig. 3) is forcing the flow to diverge, causing the formation of the two separate lobes at D and E. Ridges with a convex shape toward the east—of sedimentary origin based on their texture—lying immediately east of the volcano-shaped feature (profile C–C′) are interpreted as compressional ridges. In contrast, steep depressions are situated to the north and south of the volcano (profile B–B′), eventually forming a no-flow zone with regard to salt movement. Further indications for the importance of the local basement controlling the salt flows are ridges rotating toward the NW at the distal (NW) end of feature D. As cross section A–A′ demonstrates, the volcanic basement in the central trough is deeper toward the northwest of feature D than toward the south and the curved fabrics indicate a preferred downslope movement toward the NW. Generally, both along-slope and downslope ridges and troughs attributed to the salt flows are located either perpendicular or parallel to the seafloor gradient. This agrees with a formation induced by gravitational stresses, as would be expected from downslope-flowing salt (Mitchell et al. 2010).

Finally, it is interesting to note that the salt flow F continues beneath the top brine level (Fig. 4). This irregular topography observed close to the flow front (Fig. 4) may be related to the dissolution of evaporites (Pilcher and Blumstein 2007), contributing to the formation of the brine in the enclosed Atlantis II Deep. Similar small areas of irregular seafloor are observed on feature C (Mitchell et al. 2010).

Mechanical Behavior of Salt Flows

Introduction

The deformation mechanisms of halite (rock salt) occurring as a response to the local stress field range from cataclastic deformation (breakage) to crystal–plastic movement (recrystallization and creep), and pressure solution creep (Urai et al. 2008). Under most natural conditions, halite shows a ductile behavior when its elastic limit is exceeded. The related plastic deformation can include movement within a crystal ("dislocation creep") as well as mass transfer by diffusion ("pressure solution creep," Green 1984). Dislocation creep involves movements within the crystal lattice along glide planes that cause the formation of subgrains. It is the dominant deformation process under higher temperatures, differential stresses, and dry conditions (Urai et al. 2008). However, under low differential stresses and available interstitial water, pressure solution creep is important (De Meer et al. 2002). This type of creep involves dissolution at grain boundaries exposed to high stress, the transport of the dissolved material along the grain boundaries, and the precipitation at boundaries under low stress. Pressure solution creep can cause considerably higher strain rates than dislocation creep (Jackson and Talbot 1986). Therefore, the amount of intergrain water (Talbot and Pohjola 2009) and grain size (Urai et al. 2008) significantly influences mechanical behavior. The effectiveness of pressure solution creep increases with the amount of intergranular water and decreasing grain size (i.e., with increasing grain total surface area and decreasing diffusion distance).

The mechanical behavior of extrusive salt flows (locally called "namakiers") has been studied in southern Iran. Namakiers show varied advancement rates (Talbot and Pohjola 2009) under low differential stresses of 0.03–0.25 MPa (Wenkert 1979; Talbot and Rogers 1980). Namakiers move at several cm to m per year, but can surge with speeds of centimeters to decimeters per day during heavy rain (Jackson and Talbot 1986; Talbot et al. 2000). Correspondingly, measured strain rates vary widely between 10^{-9} and 10^{-11}. Pressure solution creep active in fine-grained mylonitic shear zones is considered the dominant deformation process involved in onshore salt flow.

Generally, strain rate due to dislocation creep for extrusive onshore salt flows follows a power law with differential stress (Schléder and Urai 2007):

$$\dot{\varepsilon}_{DC} = 8.1 \times 10^{-5} e^{(Q_{DC}/RT)} (\sigma_1 - \sigma_3)^{3.4} \qquad (1)$$

where Q_{DC} = the activation energy energy for dislocation creep ($-56,000$ J mol^{-1}), T = temperature in Kelvin, R = universal gas constant, and $\sigma_1 - \sigma_3$ = differential stress (Pa).

The strain rate for pressure solution creep (based on experiments on porous and dense polycrystalline aggregates of synthetic rock salt) may be estimated from (Schléder and Urai 2007; Urai et al. 2008):

$$\dot{\varepsilon}_{ps} = 4.7 \times 10^{-4} e^{(Q_{ps}/RT)} \frac{(\sigma_1 - \sigma_3)}{TD^3} \qquad (2)$$

where D = grain diameter (mm) and Q_{ps} = activation energy for pressure solution creep ($-24,530$ J mol^{-1}).

Equations 1 and 2 were developed for halite, but large parts of the evaporite sequence in the Red Sea are comprised of anhydrite (see DSDP core stratigraphy in Fig. 1). The mechanical behavior of anhydrite is less well understood, especially under wet conditions and low stresses and strain

rates that are expected in salt flows located at or near the surface (Dell'Angelo and Olgaard 1995; Urai et al. 2008). Available flow laws were derived at high pressures and strain rates (Dell'Angelo and Olgaard 1995; Heidelbach et al. 2001) and are likely not applicable for salt flows within the Red Sea. However, generally anhydrite is stronger than halite (Ross and Bauer 1992; Zulauf et al. 2009), so strain should be dominantly accommodated within the halite layer (Ross et al. 1987; Ross and Bauer 1992) under shear stresses parallel to the layering. Therefore, for further estimations, we consider the halite component of the evaporite sequence only.

Estimation of Stresses

The movement of submarine salt flows is a response to the acting differential stress that is determined by the density and geometry of the salt and the hemipelagic cover. The morphological features on the salt flows are either parallel or perpendicular to the direction of maximum seafloor gradient, indicating that the movement—at least of the upper part of the evaporite sequence—is driven by gravitation (tectonic forcing can be neglected). According to descriptions of the cores from DSDP Sites 225 and 227, the upper approximately 100-m evaporite sequence comprises interbedded halite and anhydrite, with minor shale (Whitmarsh et al. 1974, Fig. 1). The following estimates of the stresses within the upper evaporites are based on DSDP Site 227 in the SE wall of Atlantis II Deep. Based on the available morphological and geophysical information, this site is drilled in a salt flow snout near feature "F" in Fig. 3.

The vertical stress component σ_1 is estimated with

$$\sigma_1 = \sum_{i=1}^{\text{layer}} (\rho_i - \rho_w) g h_i \qquad (3)$$

with ρ_w: density of water (g/cm^3), ρ_{layer}: density of sediment/evaporite (g/cm^3), g: gravitational acceleration (m/s^2), and h: thickness of layers (m).

If the evaporites are assumed to behave linearly elastically and isotropically, the horizontal stress σ_3 may be roughly estimated with (Bjørlykke 2010, p. 285):

$$\sigma_3 = \frac{v}{1-v} \sigma_1 \qquad (4)$$

with v being the Poisson ratio (the ratio between extension/contraction along σ_1 and contraction/extension along σ_3). v is 0.253 for halite and 0.273 for anhydrite (Gercek 2007). Thus, the horizontal stress is approximated with 0.75 * σ_1 within the evaporite layer.

For the evaporites situated in the upper part of the stratigraphic sequence, we assume that tectonic influence is negligible and that no gliding takes place at the evaporite base (Talbot and Pohjola 2009). Further, as the pore water pressures are unknown, we cannot calculate correct effective stresses. Compacted layers of low permeability may significantly influence vertical stresses. Assuming a sediment layer depth of 150 m with density ρ of 1.6 g/cm^2, a halite thickness of 100 m with a density of 2.2 g/cm^2, a water density of 1 g/cm^3 and g = 10 m/s^2, σ_1 and σ_3 in the upper region of the evaporite sequence are 2.1, and 1.6 MPa, respectively. The differential stress $\sigma_{1 - \sigma_3}$ is then 0.5 MPa.

Discussion

Location and Thickness of the Deformation Zone

Several possible depths of the main deformation zone within the stratigraphy may occur. As the thickness of the complete evaporite sequence can exceed several kilometers and immediately outside these deeps is at least 1 km (Tramontini and Davies 1969), strain could be focused in the lower parts of the evaporite sequence. Here, higher temperature and eventual hydrothermal water supports deformation. However, this cannot be the deformation mechanism responsible for the formation of the salt flows A–F observed in the Thetis and around Atlantis II Deep (Figs. 2 and 3); the flow fronts are only several hundred meters high, and thus, movement must be located in the upper part of the evaporite sequence. Here, flow could be homogenous, with the evaporites moving en masse, as reported for some allochthonous salt sheets (Fletcher et al. 1995). For the discussion of dislocation creep, it will be assumed that the complete evaporite sequence is deforming (which likely results in an overestimation of the resulting strain rate); that is, the deforming thickness equals the vertical relief of approximately 500 m minus a hemipelagic sediment thickness of approximately 200 m.

However, movement along thin shear zones is also possible; the formation of smaller grains within shear zone mylonites would enhance the effectiveness of pressure solution creep, allowing for higher deformation rates. Indeed, an earlier analysis of DSDP Leg 23 halite samples found only minor deformation (Stoffers and Kühn 1974) in the upper 100 m of the evaporite sequence, indicating the main deformation zone may be located beneath the depth drilled by the DSDP. Shear zones may form due to synsedimentary variations of mechanical properties, e.g., due to different mineralogical compositions within the evaporite

sequence (Schléder and Urai 2007). The shear zones may further be connected to shale layers (Mitchell et al. 2010) observed, e.g., in DSDP Sites 225 and 227 (Fig. 1) within the evaporites (Whitmarsh et al. 1974) because of (a) the slow release of water from the shale due to its ongoing compaction, causing a weakening of the surrounding halite or (b) shear within the shale itself caused by high pore pressures and resulting low shear strength, existing due to the very slow drainage of water that results from the extremely low permeability of the surrounding evaporites. During the DSDP drilling campaign, shale layers were mostly reported adjacent to anhydrite, though shale adjacent to halite also exists (Stoffers and Kühn 1974). Their occurrence may also be expected in the evaporite sequence below the depth drilled by the DSDP.

Without adequate samples, it cannot be determined with certainty whether slippage within the shale layer took place. However, exceedingly high pore water pressures within the shale could cause a reduced effective stress and reduced shear strength, favoring such slippage. Generally, the rate of shale compaction is rapid at shallow burial depth and then decreases with increasing depth (Magara 1980). Commonly, the Athy equation was used to calculate the porosity–depth relationship of shale (Athy 1930):

$$\Phi = \Phi_0 e^{-cZ} \qquad (5)$$

with Φ = porosity, Φ_0 = initial porosity, c = constant [1/m], approx. 10^{-3} for marine sediments (Brückmann 1989), and Z = burial depth in m.

While the Athy equation was found to be unsatisfactory for larger burial depths (Goulty 1998; Burrus 1998), it gives reliable results for shallow burial depths of up to 1 km (Wetzel 1986; Burrus 1998).

According to Eq. 5, the porosity of shale after 280 m of burial is reduced to approx. 75 % of its initial value. The initial porosity of clayey silt to pelagic clay may be assumed to be 0.7–0.8 (Meade 1966; Einsele 1989). Assuming an original porosity of 0.75, the expected porosity at 280 m burial is 0.56, with empirical data suggesting a porosity of 0.58 (Einsele 1989).

This indicates that the shale within Site 227, with a measured porosity of 0.49 (Table 1), is not undercompacted, and water was efficiently drained. Pathways for water removal within the shale could be formed by an observed intense brecciation of the shale that was attributed to salt flowage (Stoffers and Kühn 1974), while an increase in permeability of rock salt was observed due to microcracking or small faults during deformation under low temperature and mean effective stresses (Urai et al. 1986; Schléder et al. 2008). Thus, slippage in the shale itself appears less likely. Nevertheless, higher porosity and water contents in

Table 1 Selection of porosity-depth values reported for DSDP Site 227 (Manheim et al. 1974)

Depth m	Porosity	H_2O %	Composition
252	0.006	0.2	Anhydrite
282	0.066	2.43	Anhydrite
283	0.493	22.4	Shale

anhydrite directly adjacent to the shale indicate a potential weakening of the surrounding anhydrite (Table 1)—the same may take place where halite is situated adjacent to shale. Here, the high water content would increase the efficiency of deformation by pressure solution creep.

Estimation of Strain Rates

Dislocation Creep

Strain rates due to dislocation creep were estimated using Eq. 1. Although the differential stress and the temperature both increase with depth, we use constant values to simplify the analysis. The temperature at the evaporite surface is 311 K at Site 225 and 320 K at Site 227, with a temperature gradient of 92° and 117° per kilometer depth (Girdler et al. 1974; Girdler and Whitmarsh 1974). Thus, we assume a temperature of 330 K for the upper 300 m of the evaporite sequence. With a differential stress of 0.5 MPa, dislocation creep would thus occur at $\sim 10^{-14}$ 1/s.

Pressure Solution Creep

The strain rates due to pressure solution creep were estimated using Eq. 2. The critical parameter here is the grain size D, which is poorly known and strongly dominates the pressure solution creep equation. The majority of halite sampled during the DSDP campaign was coarse grained (Stoffers and Kühn 1974), suggesting that pressure solution creep would be ineffective. However, as suggested earlier, the main deformation zone may be located beneath the evaporite sequence sampled by the DSDP. Furthermore, few areas comprising halite with 1 mm grain size exist even in the DSDP cores. Interestingly, they are located adjacent to shale layers, which include veins filled with halite precipitated from pore waters (Stoffers and Kühn 1974), an indication of solution precipitation. For comparison, halite grain sizes in onshore mylontic zones are ~ 0.6 mm (Schléder and Urai 2007). Using the differential stress of 0.5 MPa and $T = 330$ K, pressure solution should occur at strain rates of approx. 5×10^{-10} 1/s for 0.6 mm grains, 10^{-10} for 1 mm grains, and 10^{-13} for 1 cm grains.

Strain Rate Constraints

Rotation of Anhydrite Layers

Strain rates for the salt flows at the southeastern wall of Atlantis II Deep can be estimated from anhydrite layers encountered throughout the evaporites in the DSDP cores (Stoffers and Kühn 1974). If these beds were originally deposited horizontally as seems reasonable, they have subsequently been rotated between 40° to 60° at Site 227 and 10° to 25° at Site 225 (Whitmarsh et al. 1974). The rotational strain would thus be given by (Twiss and Moores 1992):

$$E_s = \tan \varphi \qquad (6)$$

Assuming that deformation started with seafloor spreading at 2.4 Ma (Stoffers and Kühn 1974), the strain rate has thus been approximately 1.5×10^{-14} 1/s at Site 227 and 4×10^{-14} 1/s at Site 225. Strain rates of these orders of magnitude agree with the estimated strain rate from dislocation creep (Fig. 5).

Seafloor Spreading Rates

Seafloor spreading at Atlantis II and Thetis Deep occurs at 12 mm/year (Chu and Gordon 1998). With a half-spreading rate of 6 mm/year, approximately 15 km of oceanic crust has been generated since the onset of seafloor spreading at 2.4 Ma as indicated by magnetic anomalies (Stoffers and Kühn 1974). Recent bathymetric data show that salt fronts advance well into the central trough at the latitude of DSDP Site 227 (feature F), in Thetis deep (feature C) and south of Atlantis II Deep (Feature D), and possibly the central axis in the intertrough areas (Augustin et al. 2014). Some of this evaporite would have dissolved [demonstrated by brine including dissolved Miocene evaporite components in Atlantis II Deep (Anschutz and Blanc 1995)], so the rate from seafloor spreading may be a minimum. On the other hand, in many areas, the flow fronts do not reach the centers of the deeps, demonstrating spatially different flow speeds. For flows advancing into the central trough the half-spreading rate are used to constrain flow speed.

Generally, the approximate evaporite flow speed may be calculated with (Twiss and Moores 1992)

Fig. 5 Comparison of pressure solution creep and dislocation creep strain rate/differential stress relationship estimated for offshore salt flows (*gray ellipsoids*), compared with data derived for onshore namakiers and domal salt (*gray rectangles*) and laboratory data. Constraints for offshore salt flows are made based on the rotation of anhydrite layers, and the local half-spreading rate. Refer to the text for further discussion. Modified from Schléder and Urai (2007)
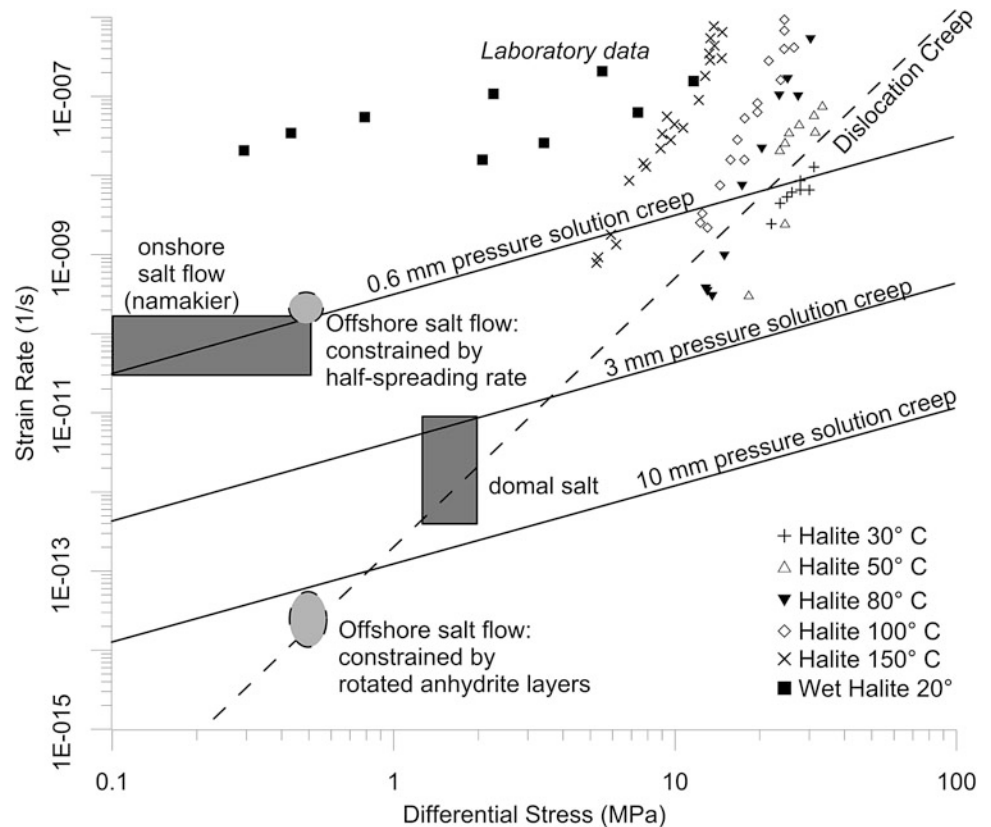
$$\text{Flow Speed [m/s]} = \text{Shear Strain Rate [1/s]}$$
$$* \text{ Shear Zone Thickness [m]} \qquad (7)$$

For dislocation creep, the shear zone thickness was (probably) overestimated at 300 m, resulting in a flow speed of 0.1 mm/year. This is less than the seafloor spreading half-rate by two orders of magnitude. For pressure solution creep, the water-influenced halite thickness adjacent to shales is less than 4 m based on measurements of water content at DSDP site 277 (Manheim et al. 1974). Assuming a 1 mm grain size [the finest halite grain size reported for the DSDP cores (Girdler and Whitmarsh 1974)] over a cumulative depth extent of 50 cm throughout the evaporite/shale sequence, the strain rate required to keep up with the half-spreading rate is 2×10^{-10} 1/s. For comparison, individual mylonitic shear zones observed onshore reach approximately 5 cm in thickness, but several exist at each namakier (Schléder and Urai 2007). While these are only rough estimates, it shows that salt flow movement speed due to pressure solution creep, with estimated strain rates between 1×10^{-10} 1/s and 5×10^{-10} 1/s (Fig. 5) for fine-grained halite, is potentially able to explain how the flows keep up with seafloor spreading at certain locations.

Conclusion

Evaporites were deposited widely during the Miocene in the area of today's Red Sea. With the onset of seafloor spreading, the evaporites lost their lateral constraint. Because halite is ductile, the evaporites started to move downslope toward the developing axial trough of the Red Sea, passively carrying a cover of hemipelagic sediments. Today, flowlike features comprising Miocene evaporites are situated on top of younger magnetic seafloor spreading anomalies. Six flowlike features on the seafloor of Thetis Deep, Atlantis II Deep, and between Atlantis II Deep and Port Sudan Deep, identified by high-resolution bathymetry and DSDP core material, are interpreted as salt flows. Steered by the configuration of the volcanic basement, individual flow lobes with heights of several hundred meters and widths of 3 and 10 km are observed. On the flow surface, downslope and along-slope ridges parallel to the local seafloor gradient have developed, presumably caused by extension of the hemiplegic sediment cover or strike-slip movement within the evaporite sequence. At the front of several salt flows, irregular seafloor points to local dissolution. In the case of Atlantis II Deep, this dissolution may contribute to the formation of the local brine. Based on the conditions known for Atlantis II Deep, differential stresses within the upper evaporites are ~ 0.5 MPa. The corresponding deformation was assumed to take place within the upper part of the

evaporite sequence, as the vertical reliefs of the salt flows do not exceed a few hundred meters. Based on physical parameters measured during the DSDP drilling campaign, strain rates due to dislocation creep were estimated to be 10^{-14} 1/s. However, this rate is low relative to rates expected of seafloor spreading, so advance of several flow lobes well into the Red Sea central trough cannot be explained by dislocation creep, but indicates the work of solution and precipitation processes ("pressure solution creep"). Depending on halite grain size, water content, and the formation of thin mylonitic shear zones (all uncertain parameters), strain rates of 10^{-10} 1/s caused by pressure solution creep appear possible, similar to deformation measured in extrusive onshore salt flows in Iran. Such strain rates result in flow speeds of several mm/year for offshore salt flows in certain locations. Thus, salt movements can potentially keep up with half-spreading rates reported for large parts of the Red Sea.

References

Anschutz P, Blanc G (1995) Origin of fluids and the evolution of Atlantis II Deep hydrothermal system, Red Sea: strontium isotope study. Geochim Cosmochim Acta 59(23):4799–4808

Athy LF (1930) Density, porosity, and compaction of sedimentary rocks. Am Assoc Pet Geol Bull 14(1):1–24

Augustin N, Colin WD, van der Zwanm F, Feldens P, Bantan R, Kwasnitschka T (2014) The rifting to spreading transition in the Red Sea. Earth Planet Sci Lett 395:217–230

Bindschadler R (1998) Monitoring ice sheet behavior from space. Rev Geophys 36(1):79–104

Bjørlykke K (2010) Petroleum geoscience: from sedimentary environments to rock physics. Springer, Berlin

Brückmann W (1989) Typische Kompaktionsabläufe mariner Sedimente und ihre Modifikation in einem rezenten Akkretionskeil (Barbados Ridge). Tübinger Geowissenschaftliche Arbeiten, Reihe A Nr. 5, 135 pp

Burrus J (1998) Overpressure models for clastic rocks, their relation to hydrocarbon expulsion: a critical reevaluation. In: Law BE, Ulmishek GF, Slavin VI (eds) Abnormal pressures in hydrocarbon environments. American Association of Petroleum Geologists Memoir, pp 35–63

Campbell I, Jacobel R, Welch B, Petterson R (2008) The evolution of surface flow stripes and stratigraphic folds within Kamb ice stream: why don't they match? J Glaciol 54(186):421–427

Chu D, Gordon RG (1998) Current plate motions across the Red Sea. Geophys J Int 135(2):313–328

Cochran JR (1983) A model for the development of the Red Sea. Am Assoc Pet Geol Bull 67:41–69

Coleman RG (1993) Geologic evolution of the Red Sea. Oxford Monogr Geol Geophys 24, 186 pp

De Meer S, Drury MR, De Bresser JHP, Pennock GM (2002) Current issues and new developments in deformation mechanisms, rheology and tectonics, vol 200. Geological Society, London, pp 1–27 (Special Publications)

Dell'Angelo L, Olgaard DL (1995) Experimental deformation of fine-grained anhydrite: evidence for dislocation and diffusion creep. J Geophys Res 100(B8):15425–15440

Einsele G (1989) In-situ water contents, liquid limits, and submarine mass flows due to a high liquefaction potential of slope sediment (results from DSDP and subaerial counterparts). Geol Rundsch 78:821–840

Fletcher CF, Hudec MR, Watson IA (1995) Salt glacier and composite sediment-salt glacier models for the emplacement and early burial of allochthonous salt sheets. In: Jackson MPA, Roberts DG, Snelson S (eds) Salt tectonics a global perspective. American Association of Petroleum Geologists Memoir, pp 77–108

Gercek H (2007) Poisson's ratio values for rocks. Int J Rock Mech Min Sci 44(1):1–13

Girdler RW, Whitmarsh RB (1974) Miocene evaporites in Red Sea cores, their relevance to the problem of the width and age of oceanic crust beneath the Red Sea. In: Whitmarsh RB, Weser OE, Ross DA (eds) Initial reports of the Deep Sea Drilling Project, vol 23. US Government Printing Office, Washington, pp 913–921

Girdler RW, Erickson AJ, Von Herzen R (1974) Downhole temperature and shipboard thermal conductivity measurements aboard d/v Glomar Challenger in the Red Sea. In: Whitmarsh RB, Weser OE, Ross DA (eds) Initial reports of the Deep Sea Drilling Project, vol 23. US Government Printing Office, Washington, pp 879–886

Glasser NF, Gudmundsson GH (2012) Longitudinal surface structures (flowstripes) on Antarctic glaciers. Cryosphere 6:383–391

Goulty NR (1998) Relationships between porosity and effective stress in shales. First Break 16(12):413–419

Green HW (1984) Pressure solution creep: some causes and mechanisms. J Geophys Res 89(B6):4313–4318

Gudmundsson GH, Raymond CF, Bindschadler R (1998) The origin and longevity of flow stripes on Antarctic ice streams. Ann Glaciol 27:145–152

Hartmann M, Scholten JC, Stoffers P, Wehner F (1998) Hydrographic structures of brine-filled deeps in the Red Sea—results from the Shaban, Kebrit, Atlantis II, and Discovery Deep. Mar Geol 144:311–330

Heidelbach F, Stretton IC, Kunze K (2001) Texture development of polycrystalline anhydrite experimentally deformed in torsion. Int J Earth Sci (Geol Rundsch) 90:118–126

Hudec MR, Jackson MPA (2006) Advance of allochthonous salt sheets in passive margins and orogens. Am Assoc Pet Geol Bull 90:1535–1564

Hudec MR, Jackson MPA (2007) Terra infirma: understanding salt tectonics. Earth-Sci Rev 82:1–28

Izzeldin AY (1987) Seismic, gravity and magnetic surveys in the central part of the Red Sea: their interpretation and implications for the structure and evolution of the Red Sea. Tectonophysics 143:269–306

Jackson MPA, Talbot CJ (1986) External shapes, strain rates, and dynamics of salt structures. Geol Soc Am Bull 97(3):305–323

Krastel S, Wynn RB, Georgiopoulou A, Geersen J, Heinrich R, Meyer M, Schwenk T (2012) Large-scale mass wasting on the northwest African continental margin: some general implications for mass wasting on passive continental margins. Adv Nat Technol Hazards Res 31:189–199

Lees GM (1927) Salzgletscher in Persien. Mitteilungen der deutschen Gesellschaft (Wien) 20:29–34

Ligi M, Bonatti E, Bortoluzzi G, Cipriani A, Cocchi L, Tontini FC, Carminati E, Ottolini L, Schettino A (2012) Birth of an ocean in the Red Sea: initial pangs. Geochem Geophys Geosyst 13(8):1–29

Magara K (1980) Comparison of porosity-depth relationships of shale and sandstone. J Pet Geol 3:175–185

Manheim FT, Dwight L, Belastock RA (1974) Porosity, density, grain density, and related physical properties of sediments from the Red Sea drill cores. In: Whitmarsh RB, Weser OE, Ross DA (eds) Initial reports of the Deep Sea Drilling Project, vol 23. US Government Printing Office, Washington, pp 887–907

Mankinen EA, Dalrymple GB (1979) Revised geomagnetic polarity time scale for the interval 0-5 m.y. B.P. J Geophys Res 84(B2):615–626

Meade RH (1966) Factors influencing the early stages of the compaction of clays and sands – review. SEPM J Sediment Res 36(4):1085–1101

Micaleff A, Masson DG, Berndt C, Stow DAV (2007) Morphology and mechanics of submarine spreading: a case study from the Storegga Slide. J Geophys Res 112(F03023):1–12

Mitchell DJW, Allen RB, Salama W, Abouzakm A (1992) Tectono-stratigraphic framework and hydrocarbon potential of the Red Sea. J Pet Geol 15(2):187–210

Mitchell NC, Ligi M, Ferrante V, Bonatti E, Rutter E (2010) Submarine salt flows in the central Red Sea. Geol Soc Am Bull 122(5–6):701–713

Mohr M, Warren JK, Kukla PA, Urai JL, Irmen A (2007) Subsurface seismic record of salt glaciers in an extensional intracontinental setting (Late Triassic of northwestern Germany). Geology 35(11):963–966

Pautot G, Auzende JM, LePichon X (1966) Continuous deep salt layer along North Atlantic margins related to early phase of rifting. Nature 227:351–354

Pilcher RS, Blumstein RD (2007) Brine volume and salt dissolution rates in Orca Basin, northeast Gulf of Mexico. Am Assoc Pet Geol Bull 91:823–833

Ross JV, Bauer SJ (1992) Semi-brittle deformation of anhydrite-halite shear zones simulating mylonite formation. Tectonophysics 213:303–320

Ross DA, Schlee J (1973) Shallow structure and geologic development of the southern Red Sea. Geol Soc Am Bull 84(12):3827–3848

Ross JV, Bauer SJ, Hansen FD (1987) Textural evolution of synthetic anhydrite-halite mylonites. Tectonophysics 140:307–326

Schléder Z, Urai JL (2007) Deformation and recrystallization mechanisms in mylonitic shear zones in naturally deformed extrusive Eocene-Oligocene rocksalt from Eyvanekey plateau and Garmsar hills (central Iran). J Struct Geol 29(2):241–255

Schléder Z, Urai JL, Nollet S, Hilgers C (2008) Solution-precipitation creep and fluid flow in halite: a case study of Zechstein (Z1) rocksalt from Neuhof salt mine (Germany). Int J Earth Sci (Geol Rundsch) 97:1045–1056

Schmidt M, Devey C, Eisenhauer A (eds) (2011) FS Poseidon Fahrtbericht/Cruise Report P408—The Jeddah Transect; Jeddah – Jeddah, Saudi Arabia, 13.01.-02.03.2011 IFM-GEOMAR Report 46

Stoffers P, Kühn R (1974) Red sea evaporites: a petrographic and geochemical study. In: Whitmarsh RB, Weser OE, Ross DA (eds) Initial reports of the Deep Sea Drilling Project, vol 23. US Government Printing Office, Washington, pp 821–847

Talbot CJ (1993) Spreading of salt structures in the Gulf of Mexico. Tectonophysics 228:151–166

Talbot CJ, Pohjola V (2009) Subaerial salt extrusions in Iran as analogues of ice sheets, streams and glaciers. Earth Sci Rev 97:155–183

Talbot CJ, Rogers EA (1980) Seasonal movements in a salt glacier in Iran. Science 208:395–397

Talbot CJ, Medvedev S, Alavi M, Shahrivar H, Heidari E (2000) Salt extrusion rates at Kuh-e-Jahani, Iran: June 1994 to November 1997, vol 174. Geological Society, London (Special Publications), pp 93–11

Tramontini C, Davies D (1969) A seismic refraction survey in the Red Sea. Geophys J Int 17(2):225–241

Twiss RJ, Moores ME (1992) Structural geology. Palgrave Macmillan, Basingstoke

Urai JL, Spiers CJ, Lister GS (1986) Weakening of rock salt by water during long-term creep. Nature 324:554–557

Urai J, Schléder Z, Spiers C (2008) Flow and transport properties of salt rocks. In: Littke R, Bayer U, Gajewski D, Nelskamp S (eds)

Dynamics of complex intracontinental basins: the Central European Basin system. Springer, Berlin, pp 277–290

Völker D, Scholz F, Geersen J (2011) Analysis of submarine landsliding in the rupture area of the 27 February 2010 Maule earthquake, Central Chile. Mar Geol 288:79–89

Wenkert DD (1979) The flow of salt glaciers. Geophys Res Lett 6 (6):523

Wetzel A (1986) Sedimentphysikalische Eigenschaften als Indikatoren für Ablagerung, Diagenese und Verwitterung von Peliten. Geowiss Fakultät Univ Tübingen, 135 pp

Whitmarsh RB, Weser OE, Ross DA (eds) (1974) Initial reports of the Deep Sea Drilling Project, vol 23. US Government Printing Office, Washington

Zulauf G, Zulauf J, Bornemann O, Kihm N, Peinl M, Zanella F (2009) Experimental deformation of a single-layer anhydrite in halite matrix under bulk constriction. J Struct Geol 31:460–474